Communication

Reconfigurable Terahertz Moiré Frequency Selective Surface Based on Additive Manufacturing Technology

Redwan Ahmad [1], Mariia Zhuldybina [1,2], Xavier Ropagnol [1,3], Ngoc Duc Trinh [2], Chloé Bois [2], Juan Schneider [4] and François Blanchard [1,*]

1   Département de Génie Électrique, École de Technologie Supérieure (ÉTS), Montréal, QC H3C 1K3, Canada
2   Institute des Communications Graphiques et de L'imprimabilité, Montréal, QC H2M 2E2, Canada
3   Institut National de la Recherche Scientifique, EMT Research Center, Varennes, QC J3X 1P7, Canada
4   Nanogrande Technologies, Montréal, QC H2N 1A4, Canada
*   Correspondence: francois.blanchard@etsmtl.ca

Abstract: We designed and fabricated a terahertz (THz) frequency selective surface (FSS) based on two distinct additive manufacturing technologies, namely, printable electronics (PE) and three-dimensional (3D) printing. Silver nanoparticle ink was printed on a polyethylene terephthalate (PET) substrate utilizing a large-scale roll-to-roll industrial PE technique with a flexographic printed unit, while the 3D-printed THz FSS was fabricated based on a powder bed fusion-selective laser melting system. The filtering characteristics of both types of FSS were verified through calculation, simulation, and experiments. Furthermore, the rotational tuning approach was applied to two identical FSS to form reconfigurable FSS which could be defined as Moiré FSS. Based on the numerical results obtained, our proposed technique which used a PE-based Moiré FSS achieves a 58% modulation depth at 0.25 THz, while experimental verification found a modulation depth of 41% at 0.22 THz, confirming that its adoption is simple and cost-effective. To the best of our knowledge, this is the first demonstration of a Moiré reconfigurable printed FSS operating in the THz region.

Keywords: terahertz frequency selective surface; printable electronics; 3D printing; moiré interference

1. Introduction

Terahertz (THz) waves, with frequencies ranging from 0.1 to 10 THz and wavelengths from 0.03 to 3 mm, have potential applications in various domains, including communications, spectroscopy, imaging, security, and medical diagnostics [1–3]. For each of these applications, it is critical to control the wavefront, and this can be done through generation and detection processes, or by inserting a filter, modulator, an absorber, etc., inside the THz path [4,5]. The frequency selective surface (FSS) is a two-dimensional frequency filter with transmission and reflection characteristics that can be designed to have high-pass, low-pass, band-pass, or band-stop characteristics [6]. Compared to metasurfaces (MS), which have sub-wavelength structures, one of the characteristics of standard FSS structures is that their unit cell size is about half that of the operational wavelength [7]. In addition to filtering properties, THz FSSs also have been reported as polarization converters [8] and absorbers [9], among other applications [10–12]. Notwithstanding this great variety of the features characterizing them, the parameters of these FSSs remain passive, and can consequently only be used for specific intended applications. A tunability technique may also be used to control the peak transmission amplitude of an FSS, resulting in the formation of a reconfigurable amplitude modulator at a certain frequency. The key materials that have been identified as potential candidates for developing THz reconfigurable modulators include semiconductors [13,14], liquid crystal [15,16], graphene [17], vanadium dioxide films [18], etc. To date, multiple tunability approaches, such as photoinduced [18], mechanical [19], electrical [20], electronical [21], and rotational [22] methods, have been used to produce modulators with active control. Impressively, over the last ten years, the

performance of the THz modulator has improved dramatically, with modulation speeds increasing from the kilohertz (kHz) to the gigahertz (GHz) [23] and modulation depths have been recorded at up to 80% [18], 90% [24], and 93% [15].

So far, the vast majority of reconfigurable THz modulators have required costly facilities such as clean rooms and multiple production steps, making them ill-suited for large-scale production. Moreover, the size of the unit cell of the FSS with an operating frequency in the lower part of the THz region (sub-millimeter/millimeter wavelength) is a few hundreds of microns, and the fact is that it is usually not necessary to use such a costly fabrication technique with sub-µm resolution for prototyping THz FSSs [11]. As an alternative, a new manufacturing method has emerged, named additive manufacturing, which can be used to fabricate different THz FSS structures with unit cell sizes measuring a few hundreds of microns. This technique is a low-cost and high-speed process and allows printing on a very large scale. It is also environmentally beneficial as it produces less raw material waste than conventional methods [25,26]. It is striking that the high precision of additive manufacturing technique, i.e., printable electronics even allows their own non-contact inline inspection by printing THz FSS [27,28]. There have already been a few reports on THz devices made via additive manufacturing, including vortex phase plates [27], diffractive THz lenses [29], gradient-refractive-index lenses [30], band-pass filters [31,32], etc. Additionally, 3D printing has been used to create a holographic metasurface antenna that operates in the GHz range [33]. Furthermore, printed flexible THz metamaterials and metasurfaces have been reported over the past few years. For instance, a THz metamaterial based on electrohydrodynamic jet printing [34] and a printed metallic checkerboard based on flexographic printing [11] have been reported. However, in these demonstrations, it should be noted that none of these devices are reconfigurable or tunable. To do so, mechanically tunable terahertz metamaterials based on a flexible PDMS substrate have been demonstrated by J. Li et al. [35], but require a standard photolithography fabrication method. To the best of our knowledge, no reports on the demonstration of a reconfigurable printed THz FSS exist in the literature to date. To achieve this, the Moiré pattern interference scheme represents an interesting and simple way to realize tunability from printed structures. Recent examples of Moiré interference have been used for electromagnetic re-configuration at the atomic scale [36], in a tunable metasurface lens [37], on a hyperbolic Moiré metasurface [38], and to control the transmission amplitude of electromagnetic waves in the GHz frequency range [22].

In the present work, we demonstrate the design, fabrication, and analysis of the filtering properties of THz FSSs produced by two different additive manufacturing approaches, i.e., printable electronics (PE) and 3D printing. The PE-based FSS was made from a silver nanoparticle ink and printed on a PET substrate, while the 3D-printed FSS was fabricated using aluminum foil. In the next step, FSSs are used to develop a reconfigurable THz FSS. To that end, the Moiré FSS was implemented using two identical FSSs based on a triangular air hole array. The proposed THz Moiré-printed FSS can be controlled by simply adjusting the rotation angle between two identical structures. In agreement with our simulations, the experimental results show a decrease in transmission from 90% to 53% at a center frequency of 0.22 THz in the case of the PE-based Moiré FSS, covering a spectral width of ~250 GHz at full width at half maximum (FWHM).

2. Modeling, Fabrication, and Experimental Characterization of THz FSSs

The FSS pattern designed in this work is similar to that reported recently in the GHz frequency range [39], but with dimensions of the air hole diameter and the distance between two holes much smaller to be suitable for THz applications. Real and microscopic images of the FSS based on PE and 3D printing are shown in Figure 1a,b, respectively. For the PE sample, they were printed on a flexible substrate using silver (Ag) nanoparticle ink (PFI-600, NovaCentrix, Austin, TX, USA) using an industrial roll-to-roll (R2R) continuous press with flexography printing units (OMET Varyflex, Lecco, Italy). With the R2R printer, a variety of plastic substrates are available, including polyethylene terephthalate (PET),

polyethylene naphthalate (PEN), and polyimide (PI). The processing temperatures for PET, PEN, and PI are 150 °C (heat stabilized), 200 °C, and 360–400 °C, respectively [40]. PEN and PI can be more expensive when compared to the PET substrate. Since the printed FSSs were dried inline with hot air at a maximum temperature of 100 °C, this allows us to choose PET as the printing substrate, which is the cheapest available and most widely used substrate. The thicknesses of the FSS pattern and PET substrate were 352 nm and 125 μm respectively, while the conductivity of the printed sample was 4.40×10^6 S/m. The diameter of the sample's air hole was ~600 μm with a distance between the centers of the two air holes (the pitch) of ~800 μm, all covering an area of 40×40 mm². A second FSS structure with the same air hole diameter and pitch size was fabricated using the 3D printing technique (printer model: MPL-1 from Nanogrande company). The main difference between the two types of fabrication is the presence of the PET substrate in the PE method while the 3D printing sample has no substrate. This one has simply a thickness of 100 μm obtained by the selective fusion by laser on metal powder bed obtaining a conductivity of approximately 2.50×10^7 S/m.
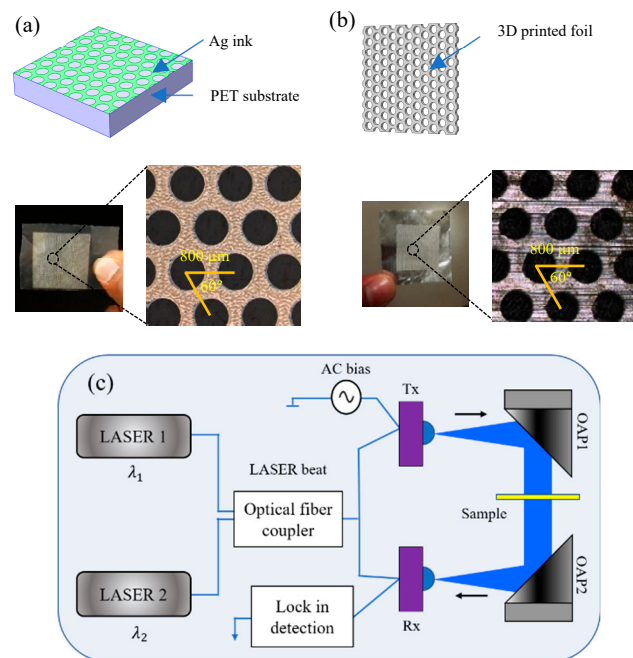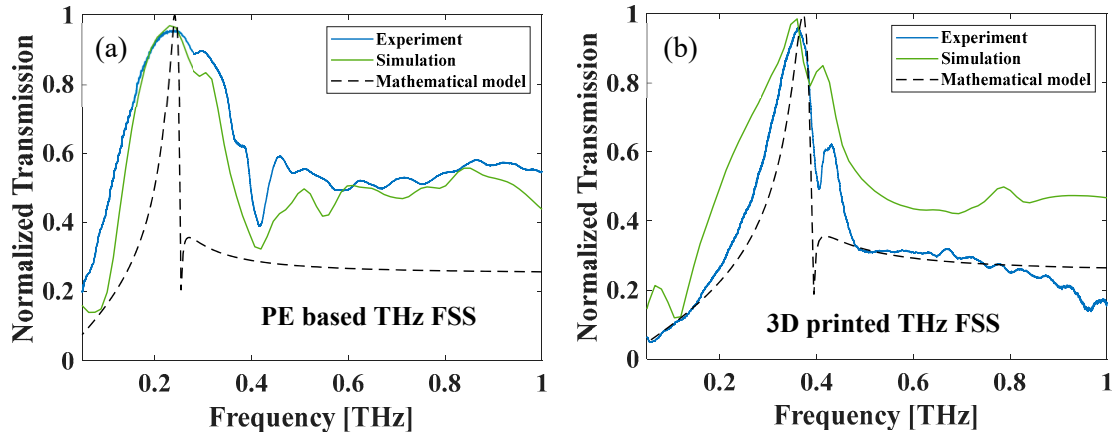

Figure 1. THz FSS (**a**) based on printable electronics using silver (Ag) ink and PET as a substrate; (**b**) based on 3D printing made from aluminum foil. (**c**) Experimental setup of CW THz spectroscopy. Here Tx, Rx, and OAP stand for transmitter, receiver, and off-axis parabolic mirror, respectively.

To investigate the features of the fabricated FSSs, we employed a commercial continuous wave (CW) THz spectroscopy system (TERASCAN 1550 from TOPTICA photonics). The experimental setup is illustrated in Figure 1c. The terahertz emitter and receiver are based on an InGaAs photodiode and InGaAs photomixer, respectively. The radiated THz waves were collimated and refocused onto the detector by a pair of 2-inch diameter and 3-inch focal length off-axis parabolic mirrors. Note that in our experiment, we used a resolution of 50 MHz to resolve the characteristics of our analyzed BPF. To extract the normalized transmission characteristics of the PE-based and 3D-printed THz BPF, the following equation was applied:

$$NT(\omega) = \left| \frac{T_{sample}(\omega)}{T_{ref}(\omega)} \right| \tag{1}$$

where $T_{sample}(\omega)$ and $T_{ref}(\omega)$ are the transmission of the sample and reference, respectively. The experimental results of PE-based and 3D-printed FSS, accordingly, are shown with

a solid blue line in Figure 2a,b. It was observed from experimental measurements that PE-based filters offered a larger bandwidth covering from 130 to 380 GHz, as compared to the 3D-printed filter, which came in at 250 to 430 GHz (i.e., at FWHM).

Figure 2. Normalized transmission as a function of frequency in the case of a single layer of THz FSS, (**a**) printable electronics-based; (**b**) 3D printed.

To confirm our experimental observation, we performed finite difference time domain (FDTD) simulations on both FSSs using Ansys Lumerical software to characterize the properties of the investigated FSSs. During the simulations, we designed and analyzed a 6 mm length by 6 mm width sample, which was positioned between the THz source and the detector section. Figure 2a,b illustrates the transmission characteristics obtained with the simulation (green line). To validate our simulation and experimental results and evaluate the filter response of both types of THz FSSs, we used the well-known numerical modeling reported by [41]. It was demonstrated that the model can accurately predict the transmission characteristics of FSS, consisting of circular apertures with triangular lattices. The transmission coefficients T can be obtained as [41]:

$$T = \frac{1}{1 - j[A + B\tanh(\beta l)]} - \frac{1}{1 - j[A + B\coth(\beta l)]} \tag{2}$$

where β is the phase constant and l is thickness of the sample. To calculate the parameters A and B as functions of hole spacing and hole size, respectively, the following Equations (3) and (4) can be applied [39,41]:

$$A = 12\left(\frac{4}{3}\left(\frac{\lambda}{d}\right)^2 - 1\right)^{\frac{1}{2}}\left[\frac{J_1'\left(\frac{4\pi a}{\sqrt{3}d}\right)}{1 - \left(\frac{4\pi a}{1.841\sqrt{3}d}\right)^2}\right]^2 - \frac{12}{\left(\frac{4}{3}\left(\frac{\lambda}{d}\right)^2 - 1\right)^{\frac{1}{2}}}\left[\frac{J_1\left(\frac{4\pi a}{\sqrt{3}d}\right)}{\frac{4\pi a}{\sqrt{3}d}}\right]^2 \tag{3}$$

$$B = 0.33\left(\frac{d}{a}\right)^2\left(\left(\frac{0.293\lambda}{a}\right)^2 - 1\right)^{\frac{1}{2}} \tag{4}$$

The circular holes' centers are separated by a distance of d, the radius of the circular hole is denoted by a, and λ stands for the wavelength. J_1 and J_1' are the first kind of Bessel function and the derivative, respectively. The phase constant can be obtained as follows:

$$\beta = \frac{2\pi}{\lambda}\left(\left(\frac{0.293\lambda}{a}\right)^2 - 1\right)^{\frac{1}{2}} \tag{5}$$

The above mathematical model is useful to accurately anticipate the transmission characteristics of a THz FSS without substrate, which is the case of the THz FSS made using 3D printing. On the other hand, for an effective prediction of the PE-based THz FSS's transmission characteristics, we ought to take into consideration the effect of the PET substrate. To this end, we replaced the λ with λ_2 in Equations (3) and (5) and defined as $\lambda_2 = \lambda \times (n/n_2)$, where n and n_2 are the refractive indices of air (1.00) and PET (1.74 at 0.5 THz) [42], respectively. As such, the calculated transmission characteristics for the two types of FSSs were evaluated using Equation (2). Figure 2a,b illustrates the transmission characteristics obtained with the mathematical model (black dotted line) and shows the calculated peak transmission frequencies for the PE and 3D-printed FSSs at 247 and 370 GHz, respectively. From the calculation, it is clear that both FSSs behave like band-pass filters (BPF). The experimental measurements and simulation results demonstrated that the peak transmission frequency of the PE-based THz BPF is at a lower frequency region as compared to the 3D-printed THz BPF due to the PET substrate. The peak transmission frequency for a single PE-based THz filter was determined to be 228, 247, and 235 GHz from simulation, calculation, and measurement, respectively. Similarly, the peak transmission frequency of a single 3D-printed THz filter obtained by simulation, calculation, and measurement are 360, 370, and 365 GHz, respectively. In Figure 2, we can see from experiments that the 3D-printed THz BPF provides a sharper transmission with a higher quality factor than the PE-based THz BPF. In addition, the stopband is exactly the same as the calculated value and more pronounced than that obtained with the PE filter. This difference in stopband performance can be explained by the larger amount of conductive material in the case of the 3D-printed sample as compared to the PE sample. In terms of peak frequency transmission, predicted filter responses for both types of filters were fairly comparable to those obtained from simulations and experiments. However, there are some apparent differences among simulated, calculated, and measured results in terms of bandwidth (BW). Particularly in the case of PE-based THz filters, a significant difference in BW was found. One reason for this discrepancy could be related to the absorption characteristics of THz waves in the PET substrate, which were not taken into account in the numerical modeling. The comparison between the PE-based and 3D-printed THz FSS in terms of several design and output parameters is presented in Table 1.

Table 1. Comparison between PE-based and 3D-printed THz FSS.

Parameters	PE-Based THz FSS	3D-Printed THz FSS
Lattice type	Triangular	Triangular
Fabrication method	R2R flexography	Powder bed fusion-selective laser melting system
Material	Ink: Ag Substrate: PET	Aluminum foil
Thickness	Ink: 352 nm Substrate: 125 µm	100 µm
Conductivity	4.40×10^6 S/m	2.50×10^7 S/m
Peak resonance frequency (experimental)	0.235 THz	0.365 THz
Bandwidth (experimental)	250 GHz	180 GHz

3. Analysis of Moiré THz Printed FSS

To study the Moiré interference effect, the simulation was performed while stacking two identical BPFs made from printed FSSs, with the orientation of the second one being changed relative to the first, with a rotation angle ranging from 0° to 90°, with a 10° step. It can clearly be seen that as the superposition angle increases, the number of smaller groups with new periodic patterns also increases because of the geometric design of the hexagonal air-hole array. Thus, two identical THz FSS are being used to form reconfigurable THz FSS. From Figure 3, it is obvious that the patterns for the 40°, 50°, and 60° rotations look like those for the 20°, 10°, and 0° rotations, respectively. Similarly, the Moiré patterns for the

70°, 80°, and 90° rotations are symmetrical with the 10°, 20°, and 30° rotations, respectively. Clearly, beyond the 30° rotation angle, the Moiré patterns repeat symmetrically, which is why we evaluated the azimuthal response of the THz transmission from a 0° to a 30° rotation angle, with a 10° step. PET was taken into consideration as a substrate of the analyzed FSS.
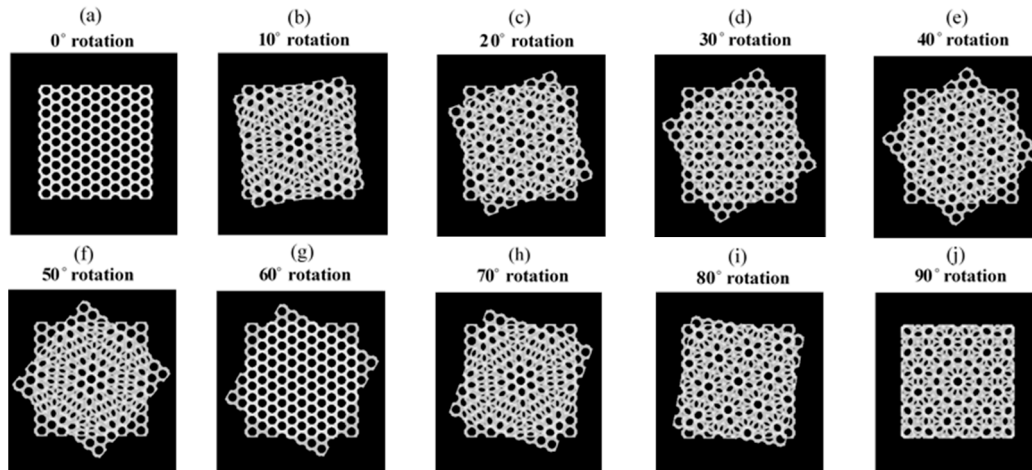

Figure 3. Simulated Moiré pattern images for the rotation angle of (**a**) 0°; (**b**) 10°; (**c**) 20°; (**d**) 30°; (**e**) 40°; (**f**) 50°; (**g**) 60°; (**h**) 70°; (**i**) 80°; (**j**) 90°.

Figure 4a–d shows the corresponding electric field distribution in the near-field for different rotation angles. The 2D simulated electric field distribution was obtained by placing the frequency domain field and power monitor in the near-field for different rotation angles. It is noteworthy that as the rotation angle was changed from 0° to 30°, unique Moiré patterns were observed with distinct field distributions, i.e., the spatiotemporal electromagnetic responses. Additionally, to evaluate the performances of the proposed THz amplitude modulator, the modulation depth needed to be calculated for various rotation angles at one fixed frequency, which was determined as the operating frequency where the maximum transmissions occur when the two samples are rotated with a 0° angle. The modulation depth (*MD*) is defined as follows:

$$MD(\%) = \frac{T_0(\omega) - T_x(\omega)}{T_0(\omega)} \times 100\% \qquad (6)$$

where $T_0(\omega)$ and $T_x(\omega)$ are the normalized transmission of the 0° and x° rotation, respectively, at the operating frequency (ω). Figure 5a shows the simulated normalized transmission at various rotation angles. As can be seen in the figure, the peak normalized transmission gradually decreases when the second sample is rotated from 0° to 20°, and for a 30° rotation angle, the normalized transmission is again increased with respect to the 20° rotation. It is also worth noting that the maximum expected transmission peak for the 0°, 10°, 20°, and 30° rotation angles are 97%, 70%, 48%, and 58%, respectively. The maximum transmission peak was obtained for a 0° rotation at 0.25 THz, which is hereafter called the operating frequency to calculate the modulation depth for different rotation angles. Accordingly, the normalized transmission decreased from 93% to 39% at 0.25 THz when the rotation angle was adjusted from 0° to 20°, resulting in a modulation depth of 58% (see Figure 5b-left axis). Likewise, the modulation depth was calculated as 28% and 46% for the 10° and 30° rotation angles, respectively (see Figure 5b-right axis). Changes in bandpass filtering bandwidth could also be seen when the second sample was rotated from 0° to 30°. At FWHM, the filtering bandwidth became 238, 175, 230, and 160 GHz for 0°, 10°, 20°, and 30° rotation angles, respectively. It can also be seen that the peak resonance frequency is also shifted towards the higher frequency range due to the geometry of the Moiré pattern

for different rotation angles. The corresponding peak resonance frequency becomes 0.241, 0.254, 0.275, and 0.280 THz for the 0°, 10°, 20°, and 30° rotation angles, respectively. From both the FWHM bandwidth and peak resonance frequency for different rotation angles, it is evident that the rotation angle of 30° exhibits the highest *Q* factor among all the rotation angles, with the FWHM bandwidth dropping to its lowest value (160 GHz). As mentioned earlier, the Moiré patterns repeat symmetrically after a 30° rotation. To validate this, we studied the modulation depths over an azimuthal range up to 120°, as shown in Figure 5c. From this figure, it can easily be estimated that a total of five "zero" modulation depths with 60° intervals will be obtained for a full 360° rotation, in agreement with the hexagonal array of the designed filters. Finally, the simulation clearly showed that the transmission of the incident THz wave could thus be controlled at the operating frequency by employing only the rotational tuning approach.
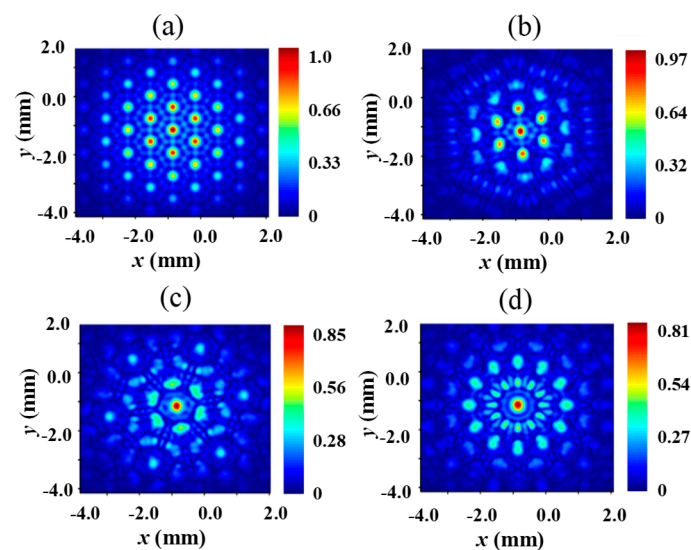

Figure 4. Numerically obtained electric field distribution in near-field in the case of: (**a**) 0° rotation; (**b**) 10° rotation; (**c**) 20° rotation; (**d**) 30° rotation.

In order to validate our simulation results, we studied the visual effect of Moiré interference patterns using a 633 nm diode mounted on a 2f imaging system and coupled to a CMOS camera (model: DCC3260M). To form a Moiré FSS, we employed two identical PE-based FSSs positioned as close as possible to each other. It should be recalled that two PE-based samples were arranged such that the conductive ink parts touched one another, and on the two exterior surfaces are PET substrates. The alignment of the two printed samples was also performed using a 2f imaging system, with one held fixed in one sample holder and the other with a rotatable mount to rotate at some fixed angles. The respective Moiré patterns obtained for 10°, 20°, and 30° angle rotations with the printed samples are shown in Figure 6a–c, respectively. It can be seen that the simulated and experimental images are consistent and quite similar (e.g., see between Figures 4a–d and 6a–c).

In the following step, the normalized transmissions for various rotation angles were measured by using two PE-based THz FSSs (shown in Figure 6d). At 0.22 THz, we extracted the normalized transmission for 0°, 10°, 20°, and 30° rotation angle and obtained 90%, 66%, 53%, and 58%, respectively. Their respective modulation depths were calculated using Equation (6). Furthermore, from Figure 6d, it can be seen that as the rotation angle changed from 0° up to 30°, significant variations in the transmission and modulation depths were observed. The lowest transmission of an incident THz wave obtained at 0.22 THz for the 20° rotation angle was 53%, corresponding to a maximum modulation depth of 41%. Additionally, for the 10° and 30° rotation angles the modulation depth was calculated as 26% and 35%, respectively. It can be seen that our experimental results show some deviations from the simulation results. From our observations, three factors are critical

in this experiment based on PE-based samples: (1) a presence of air gap spacing between the two samples, (2) a hole-to-hole misalignment during the superposition of the two samples, and (3) a reproducibility error of the identical fabricated samples (although in the case of printable electronics-based samples, this error is insignificant). These three factors could explain the difference between the experimental results and a perfect situation (simulation). Despite the differences in values between the simulated and the experimental transmission and modulation depths, the general behavior was the same in both cases, and we obtained a maximum modulation depth for the 20° rotation (as shown in Figure 6e), in agreement with the simulation. One of the major advantages of our analyzed printed Moiré reconfigurable THz FSS is that no external stimulus, such as a bias voltage or photoexcitation, needs to be applied in order to achieve the tunability of the transmitted wave. To achieve reconfigurability, two samples could simply be superposed over one another, with only one layer needing to be rotated relative to the other. Furthermore, this rotation can be done and controlled remotely with a motorized translation stage to make THz FSS become active.
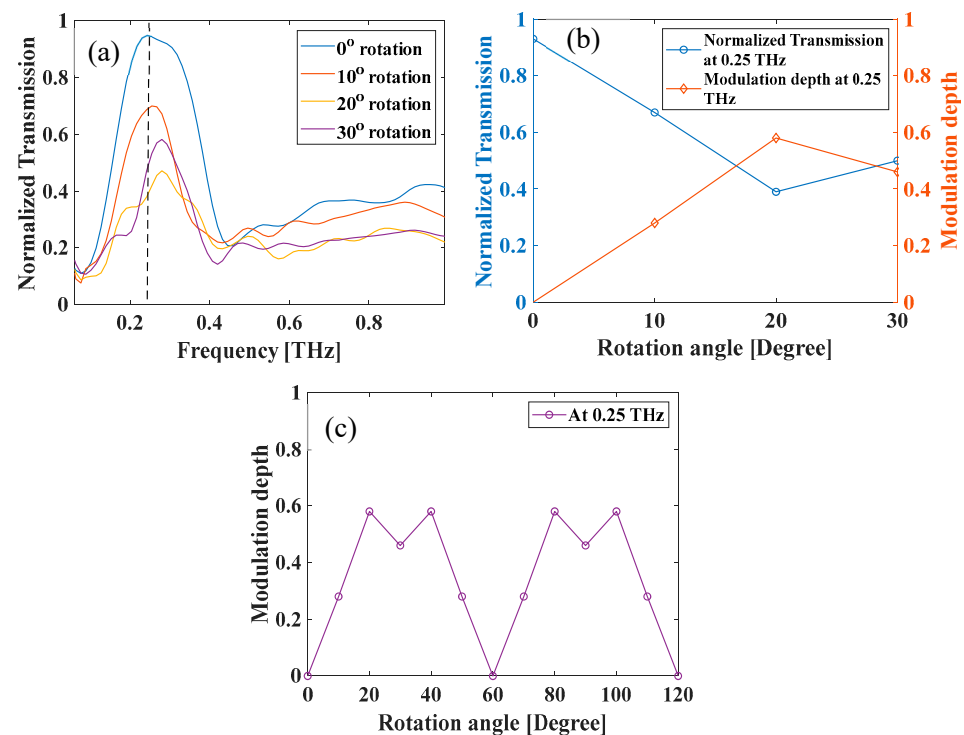
Figure 5. (**a**) Simulated normalized transmission for different rotation angles as 0°, 10°, 20°, and 30°; (**b**) normalized transmission (blue line) and modulation depth (orange line) as a function of rotation angles at operating frequency of 0.25 THz; (**c**) simulated modulation depth as a function of rotation angles from 0° to 120° at 0.25 THz.

Additionally, we used two FSSs which were 3D printed, as shown in Figure 1b, to characterize the Moiré interference effect by varying the rotation angle between the samples, just as we did with samples made of PE. However, the high malleability and non-flat surface of the 3D-printed samples made it difficult to superimpose them on each other, and this surface variation resulted in a significant misalignment error, i.e., the holes did not form the desired interference patterns. Because of their non-flat surface, the analyzed 3D printed Moiré FSS was not performed effectively in terms of modulation depth (figure not shown here) when compared to PE-based Moiré FSS. Moreover, the aforementioned problems could be minimized by increasing the printing layers to make it flat surface in the case of 3D-printed FSSs in order to achieve the desired modulation depth.
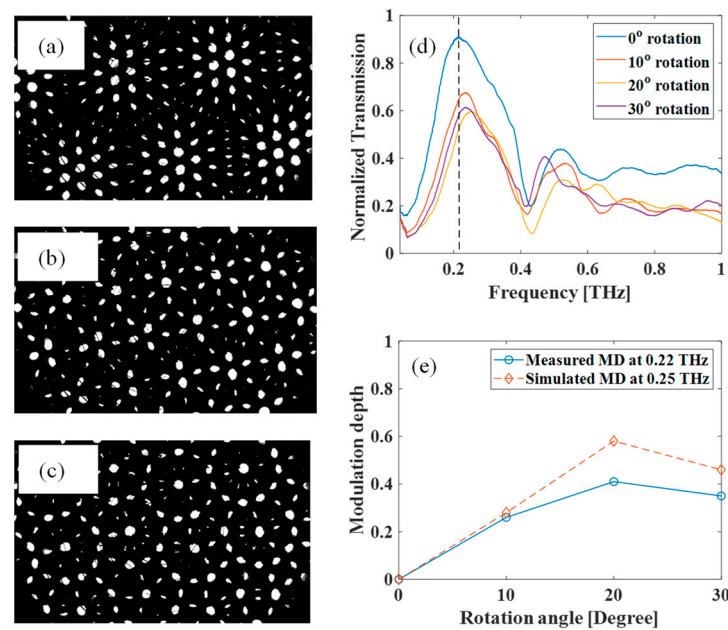
Figure 6. Moiré pattern image taken using 2f imaging system for (**a**) 10° rotation; (**b**) 20° rotation; (**c**) 30° rotation. (**d**) Experimental normalized transmission as a function of frequency for different rotation angles. (**e**) Obtained modulation depth in the case of simulation and measured findings as a function of rotation angles.

4. Conclusions

In conclusion, we analyzed THz band-pass filters fabricated based on two different additive manufacturing technologies. It can be noted that both technologies allow the efficient manipulation of THz waves, i.e., band-pass filtering through the printing of FSSs. It can be seen that 3D-printed THz BPF offers a narrow pass-band i.e., a higher quality factor as compared to the PE-based analyzed THz BPF. Additionally, the implementation of the Moiré interference technique based on the printed FSSs can potentially open up new possibilities for the mass production of reconfigurable THz FSS at lower cost. Remarkably, the maximum modulation depth obtained experimentally at 0.22 THz is 41% for a 20° rotation, which is relatively adjacent to the expected value obtained by simulation, which was 58% at 0.25 THz in the case of PE-based Moiré FSS. By improving the alignment and limiting the air gap between the two samples, the discrepancy between the simulation and the experimental results could be minimized and the modulation depth could be improved. This validates the usefulness of the proposed printing technology and of the Moiré THz reconfigurable FSS.

Author Contributions: Conceptualization, R.A., M.Z. and F.B.; experimental validation, R.A., M.Z. and X.R.; simulation investigation, R.A.; resources, F.B.; supervision, F.B.; writing—review and editing, R.A., M.Z., X.R., N.D.T., C.B., J.S. and F.B. The manuscript was written through contributions by all the authors. All authors have read and agreed to the published version of the manuscript.

Institutional Review Board Statement: Not applicable.

Informed Consent Statement: Not applicable.

Data Availability Statement: Data underlying the results presented in this paper are not publicly available at this time but may be obtained from the authors upon reasonable request.

References

1. Tonouchi, M. Cutting-edge terahertz technology. *Nat. Photon* **2007**, *1*, 97–105. [CrossRef]
2. Wu, J.-Y.; Xu, X.-F.; Wei, L.-F. Active metasurfaces for manipulatable terahertz technology. *Chin. Phys. B* **2020**, *29*, 094202. [CrossRef]
3. Zhao, F.; Li, Z.; Li, S.; Dai, X.; Zhou, Y.; Liao, X.; Cao, J.C.; Liang, G.; Shang, Z.; Zhang, Z.; et al. Terahertz metalens of hyper-dispersion. *Photon- Res.* **2022**, *10*, 886. [CrossRef]
4. Luo, L.; Chatzakis, I.; Wang, J.; Niesler, F.B.P.; Wegener, M.; Koschny, T.; Soukoulis, C.M. Broadband terahertz generation from metamaterials. *Nat. Commun.* **2014**, *5*, 3055. [CrossRef]
5. Siday, T.; Vabishchevich, P.P.; Hale, L.L.; Harris, C.T.; Luk, T.S.; Reno, J.L.; Brener, I.; Mitrofanov, O. Terahertz Detection with Perfectly-Absorbing Photoconductive Metasurface. *Nano Lett.* **2019**, *19*, 2888–2896. [CrossRef]
6. Anwar, R.S.; Mao, L.; Ning, H. Frequency Selective Surfaces: A Review. *Appl. Sci.* **2018**, *8*, 1689. [CrossRef]
7. Ebrahimi, A.; Nirantar, S.; Withayachumnankul, W.; Bhaskaran, M.; Sriram, S.; Al-Sarawi, S.F.; Abbott, D. Second-order terahertz bandpass frequency selective surface with miniaturized elements. *IEEE Trans. Terahertz Sci. Technol.* **2015**, *5*, 761–769. [CrossRef]
8. Euler, M.; Fusco, V.; Cahill, R.; Dickie, R. 325 GHz single layer sub-millimeter wave FSS based split slot ring linear to circular polarization convertor. *IEEE Trans. Antennas Propag.* **2010**, *58*, 2457–2459. [CrossRef]
9. Cheng, Y.Z.; Withayachumnankul, W.; Upadhyay, A.; Headland, D.; Nie, Y.; Gong, R.Z.; Bhaskaran, M.; Sriram, S.; Abbott, D. Ultrabroadband plasmonic absorber for Terahertz waves. *Adv. Opt. Mater.* **2014**, *3*, 376–380. [CrossRef]
10. Xia, B.G.; Zhang, D.H.; Meng, J.; Huang, J.; Yao, C.F.; Zhang, J.S. Terahertz FSS for space borne passive remote sensing application. *Electron. Lett.* **2013**, *49*, 1398–1399. [CrossRef]
11. Zhuldybina, M.; Ropagnol, X.; Bois, C.; Zednik, R.J.; Blanchard, F. Printing accuracy tracking with 2D optical microscopy and super-resolution metamaterial-assisted 1D terahertz spectroscopy. *npj Flex. Electron.* **2020**, *4*, 21. [CrossRef]
12. Silalahi, H.M.; Chen, Y.-P.; Shih, Y.-H.; Chen, Y.-S.; Lin, X.-Y.; Liu, J.-H.; Huang, C.-Y. Floating terahertz metamaterials with extremely large refractive index sensitivities. *Photonics Res.* **2021**, *9*, 1970–1978. [CrossRef]
13. Chen, H.-T.; Padilla, W.J.; Zide, J.M.O.; Gossard, A.C.; Taylor, A.J.; Averitt, R.D. Active terahertz metamaterial devices. *Nature* **2006**, *444*, 597–600. [CrossRef]
14. Jia, W.; Sensale-Rodriguez, B. Terahertz metamaterial modulators based on wide-bandgap semiconductor lateral Schottky diodes. *Opt. Mater. Express* **2022**, *12*, 940–948. [CrossRef]
15. Isić, G.; Vasić, B.; Zografopoulos, D.C.; Beccherelli, R.; Gajić, R. Electrically tunable critically coupled terahertz metamaterial absorber based on nematic liquid crystals. *Phys. Rev. Appl.* **2015**, *3*, 064007. [CrossRef]
16. Liu, S.; Xu, F.; Zhan, J.; Qiang, J.; Xie, Q.; Yang, L.; Deng, S.; Zhang, Y. Terahertz liquid crystal programmable metasurface based on Resonance switching. *Opt. Lett.* **2022**, *47*, 1891–1894. [CrossRef]
17. Yatooshi, T.; Ishikawa, A.; Tsuruta, K. Terahertz wavefront control by tunable metasurface made of graphene ribbons. *Appl. Phys. Lett.* **2015**, *107*, 053105. [CrossRef]
18. Zhang, Y.; Qiao, S.; Sun, L.; Shi, Q.W.; Huang, W.; Li, L.; Yang, Z. Photoinduced active terahertz metamaterials with nanostructured vanadium dioxide film deposited by sol-gel method. *Opt. Express* **2014**, *22*, 11070–11078. [CrossRef]
19. Pryce, I.M.; Aydin, K.; Kelaita, Y.A.; Briggs, R.M.; Atwater, H.A. Characterization of the tunable response of highly strained compliant optical metamaterials. *Philos. Trans. R. Soc. A Math. Phys. Eng. Sci.* **2011**, *369*, 3447–3455. [CrossRef]
20. Yang, R.; Lou, J.; Zhang, F.; Zhu, W.; Xu, J.; Cai, T.; Fu, Q.; Li, H.; Fan, Y. Active control of terahertz toroidal excitations in a hybrid metasurface with an electrically biased silicon layer. *Adv. Photonics Res.* **2021**, *2*, 2100103. [CrossRef]
21. Wang, G.; Tian, H.; Wang, J.; Li, S.; Guo, W.; Zhou, Z. Electronically controlled flexible terahertz metasurface based on the loss modulation of Strontium Titanate. *Opt. Lett.* **2022**, *47*, 94–97. [CrossRef]
22. Han, J.-H.; Kim, I.; Ryu, J.-W.; Kim, J.; Cho, J.-H.; Yim, G.-S.; Park, H.-S.; Min, B.; Choi, M. Rotationally reconfigurable metamaterials based on moiré phenomenon. *Opt. Express* **2015**, *23*, 17443–17449. [CrossRef]
23. Zhang, Y.; Qiao, S.; Liang, S.; Wu, Z.; Yang, Z.; Feng, Z.; Sun, H.; Zhou, Y.; Sun, L.; Chen, Z.; et al. Gbps Terahertz External Modulator Based on a Composite Metamaterial with a Double-Channel Heterostructure. *Nano Lett.* **2015**, *15*, 3501–3506. [CrossRef]
24. Isic, G.; Sinatkas, G.; Zografopoulos, D.C.; Vasic, B.; Ferraro, A.; Beccherelli, R.; Kriezis, E.E.; Belic, M. Electrically tunable metal–semiconductor–metal terahertz metasurface modulators. *IEEE J. Sel. Top. Quantum Electron.* **2019**, *25*, 1–8. [CrossRef]
25. Castro-Camus, E.; Koch, M.; Hernandez-Serrano, A.I. Additive manufacture of photonic components for the Terahertz Band. *J. Appl. Phys.* **2020**, *127*, 210901. [CrossRef]
26. Irimia-Vladu, M.; Glowacki, E.D.; Sariciftci, N.S.; Bauer, S. Green materials for Electronics. *Wiley-VCH* **2017**, *101*, 75.
27. Zhuldybina, M.; Ropagnol, X.; Trudeau, C.; Bolduc, M.; Zednik, R.; Blanchard, F. Contactless in situ electrical characterization method of printed electronic devices with terahertz spectroscopy. *Sensors* **2019**, *19*, 444. [CrossRef]

28. Zhuldybina, M.; Ropagnol, X.; Blanchard, F. Towards in-situ quality control of conductive printable electronics: A review of possible pathways. *Flex. Print. Electron.* **2021**, *6*, 043007. [CrossRef]

29. Furlan, W.D.; Ferrando, V.; Monsoriu, J.A.; Zagrajek, P.; Czerwińska, E.; Szustakowski, M. 3D printed diffractive terahertz lenses. *Opt. Lett.* **2016**, *41*, 1748–1751. [CrossRef]

30. Hernandez-Serrano, A.I.; Weidenbach, M.; Busch, S.F.; Koch, M.; Castro-Camus, E. Fabrication of gradient-refractive-index lenses for terahertz applications by three-dimensional printing. *J. Opt. Soc. Am. B* **2016**, *33*, 928–931. [CrossRef]

31. Ahmad, R.; Zhuldybina, M.; Ropagnol, X.; Blanchard, F. Terahertz metasurface based on additive manufacturing technology. In Proceedings of the 2022 Photonics North (PN), Niagara Falls, ON, Canada, 24–26 May 2022; p. 1. [CrossRef]

32. Sushko, O.; Pigeon, M.; Donnan, R.S.; Kreouzis, T.; Parini, C.G.; Dubrovka, R. Comparative study of sub-THz FSS filters fabricated by inkjet printing, microprecision material printing, and photolithography. *IEEE Trans. Terahertz Sci. Technol.* **2017**, *7*, 184–190. [CrossRef]

33. Yurduseven, O.; Ye, S.; Fromenteze, T.; Wiley, B.J.; Smith, D.R. 3D conductive polymer printed metasurface antenna for Fresnel focusing. *Designs* **2019**, *3*, 46. [CrossRef]

34. Yudistira, H.T.; Tenggara, A.P.; Nguyen, V.D.; Kim, T.T.; Prasetyo, F.D.; Choi, C.G.; Choi, M.; Byun, D. Fabrication of terahertz metamaterial with high refractive index using high-resolution electrohydrodynamic jet printing. *Appl. Phys. Lett.* **2013**, *103*, 211106. [CrossRef]

35. Li, J.; Shah, C.M.; Withayachumnankul, W.; Ung, B.S.-Y.; Mitchell, A.; Sriram, S.; Bhaskaran, M.; Chang, S.; Abbott, D. Mechanically tunable terahertz metamaterials. *Appl. Phys. Lett.* **2013**, *102*, 121101. [CrossRef]

36. He, F.; Zhou, Y.; Ye, Z.; Cho, S.-H.; Jeong, J.; Meng, X.; Wang, Y. Moiré patterns in 2D materials: A Review. *ACS Nano* **2021**, *15*, 5944–5958. [CrossRef]

37. Iwami, K.; Ogawa, C.; Nagase, T.; Ikezawa, S. Demonstration of focal length tuning by rotational varifocal moiré metalens in an IR-a wavelength. *Opt. Express* **2020**, *28*, 35602–35614. [CrossRef] [PubMed]

38. Liu, Y.; Ouyang, C.; Xu, Q.; Su, X.; Yang, Q.; Ma, J.; Li, Y.; Tian, Z.; Gu, J.; Liu, L.; et al. Moiré-driven electromagnetic responses and magic-angle in sandwiched hyperbolic metasurface. *Photonics Res.* **2022**, *10*, 2056–2065. [CrossRef]

39. Kim, D.H.; Mohyuddin, W.; Woo, D.S.; Choi, H.C.; Kim, K.W. Design of a 75–140 GHz high-pass printed circuit board dichroic filter. *Rev. Sci. Instrum.* **2017**, *88*, 034704. [CrossRef]

40. Park, J.W.; Kang, B.H.; Kim, H.J. A review of low-temperature solution-processed metal oxide thin-film transistors for Flexible Electronics. *Adv. Funct. Mater.* **2019**, *30*, 1904632. [CrossRef]

41. Chen, C.-C. Transmission of microwave through perforated flat plates of finite thickness. *IEEE Trans. Microw. Theory Tech.* **1973**, *21*, 1–6. [CrossRef]

42. Jin, Y.-S.; Kim, G.-J.; Jeon, S.-G. Terahertz dielectric properties of polymers. *J. Korean Phys. Soc.* **2006**, *49*, 513–517.